Check for updates

AGU ADVANCING EARTH AND SPACE SCIENCE

Water Resources Research

RESEARCH ARTICLE
10.1029/2022WR031938

Capillary Water in 2-D Drying-Cracking Soil Sub-Grain Models: Morphology and Kinematics of Evaporation and Haines Jumps

Boleslaw Mielniczuk[1] and **Tomasz Hueckel**[1,2]

[1]Multiphysics Geomechanics Lab, Duke University, Durham, NC, USA, [2]Civil and Environmental Engineering Department, Duke University, Durham, NC, USA

Key Points:

- Long cylindrical 3-grain capillary bridges show 2-D meniscus evolution with jumps
- Evaporating menisci evolve nonsymmetrically, flatten at contacts and sharpen at tips, constrained by grain configuration before the throat
- Meniscus accelerates and jumps when its tip crosses the throat, then slows down and splits when entering in contact with another grain solid surface

Supporting Information:

Supporting Information may be found in the online version of this article.

Correspondence to:

B. Mielniczuk,
boleslaw.mielniczuk@duke.edu

Citation:

Mielniczuk, B., & Hueckel, T. (2022). Capillary water in 2-D drying-cracking soil sub-grain models: Morphology and kinematics of evaporation and Haines jumps. *Water Resources Research*, *58*, e2022WR031938. https://doi.org/10.1029/2022WR031938

Received 5 JAN 2022
Accepted 19 AUG 2022

© 2022. American Geophysical Union. All Rights Reserved.

Abstract Morphing of capillary water during the drying of a cluster of three wet grains is imaged and measured. The uniqueness of the tests is in the grains being long cylinders to make the system as close to a 2-D one as possible. In this way, the Laplace pressure depends on the only one curvature of the meniscus, which can easily be followed and is continuously image processed. The motion of liquid/gas interface, and its rate, as well as of contact angle and perimeter, are also monitored. The drying water body has been known to undergo two modes of re-morphing: a slow, evaporation rate-controlled one and a fast, inertia-driven instabilities of the interfaces. Two particular forms of dynamic re-morphing are being followed: one, called classically an "air entry," which is a meniscus jump before its approaching the throat between the top and a bottom grain and another jump of the bottom contact, with a splitting of the meniscus into two between only two of the three grains. Associated dynamic variables, capillary pressure, and surface tension forces developing prior to and in conjunction with the instabilities of the menisci are presented in a companion paper by Hueckel et al. (2022, https://doi.org/10.1029/2022WR031938).

1. Introduction

This paper addresses certain key elements of drying-cracking process of initially wet granular materials. Drying is understood here as a series of various processes driven by but not necessarily limited to pore water evaporation. The paper focuses on one possible mechanism of drying cracking onset resulting from instability episodes referred to in soil physics and soil mechanics as "air entry." It has been shown in the past that the onset of drying-cracking correlates with the first air entry that is recognized as instability of the meniscus and the corresponding adhesion force value jump occurring at the start of desaturation (Haines, 1928; Scherer, 1992). Finally, the energy released during the individual unstable force jumps is believed to be transmitted to deform the solid skeleton and partially dissipate during the macroscopic process of cracking (Holtzman & Juanes, 2010; Hueckel et al., 2014; Mielniczuk et al., 2021; Peron et al., 2009, 2013). The meniscus instabilities are hence seen as perturbations, creating conditions for drying cracking. Both air entry and drying-cracking are potential sources of changes in permeability of hydraulic barriers made of geomaterials. The mechanisms of such changes are deemed similar to those, either chemical or physical ones, affecting contaminated or heated clays where the immobile adsorbed water is being re-morphed, changing the hydraulic conductivity, see for example, Ma & Hueckel, 1992; Hueckel et al. (1997); Hueckel & Pellegrini, (2002).

Drying-cracking is considered one of the possible adverse effects of heating and/or of forced ventilation of geological barriers (including engineered and/or of natural clays) in nuclear, hazardous, and even municipal waste disposal technology. Drying-cracking was observed in situ tests of heated clay (AECL, 1997). More recently, Mayor et al. (2007), reported a similar 30 cm thick cracked clay layer in ventilation tests at the Mont Terri underground lab. A complex array of cracks was also reported arising in heated block samples of argillite (Hedan et al., 2012). At a natural analog site near clay/basalt contact a vast area of microcracking was reported linked to an extensive evaporation (Benvegnú et al. (1988), see also Gera et al. (1996), Hueckel & Pellegrini, 2002).

This paper reports the results of sub-grain scale experiments on the evaporation of pore water from capillary clusters of a few grains. Substantial progress has recently been made in numerical modeling of invasion of air into fluid permeated macroscopic granular medium with some pore-scale features at a many-pore scale, or a few-pore scale (see e.g., Armstrong et al., 2015; Gagneaux et al., 2017; Melnikov et al., 2015; Richefeu et al., 2009; Moebius & Or, 2012; Semprebon et al., 2016; Wang et al., 2017; Zhao et al., 2019). This work focuses on a sub-grain scale meniscus,

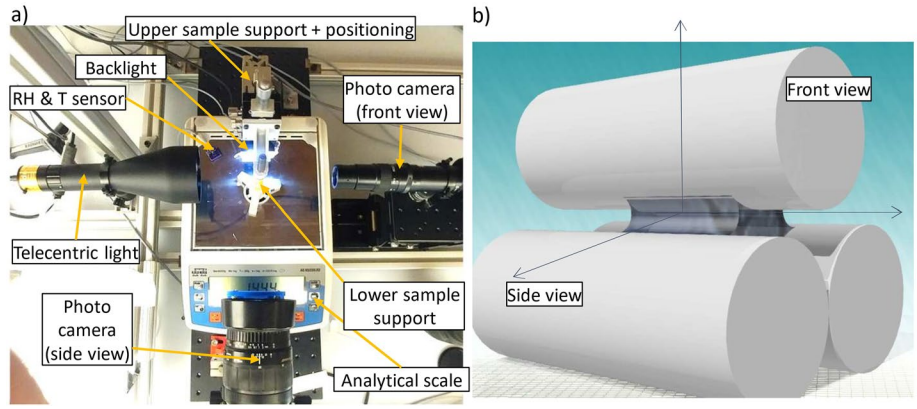

Figure 1. (a) Photo of the apparatus developed for cylindrical capillary bridge testing, and (b) a schematic view of cylindrical grain sample: initial side-length of the capillary bridge: 8.57 mm; grain diameter: 3.96 mm; grain separation: 0.434 mm; initial water volume: 10 μl.

with its main parts consisting of image collection, processing and analysis of the boundaries of the capillary water body, and their propagation. During evaporation, as liquid mass is being converted into gas at the liquid/gas interface, or meniscus, the latter one propagates incrementally with the rate of evaporation The dynamics and instabilities of menisci are addressed separately (Hueckel et al., 2022). How the interfaces actually translate, rotate and take on a different form is still an open question, both from the physics and mathematics points of view (see e.g., Scardovelli & Zaleski, 1999; Yang et al., 2018) in problems like droplet and capillary bridge drying.

In reference to meniscus evolution, we deliberately avoid a term "displacement," or "deformation," as at each moment in time, the meniscus is made of a collection of different material points at the fluid/gas interface, while the current meniscus points transition to become a part of the gas phase, over a time increment. We use the term "propagation" to describe the motion and change in the shape of meniscus. A mathematical effort to follow the evolution of the meniscus during evaporation of a capillary bridge between solid grains needs to overcome a difficulty resulting from the fact that the boundary of the liquid is not known a priori and it is moving, see for example, Yang et al. (2018). Evaporation has been seen to produce pressure gradients within the water bridge and a consequent liquid flow, as a result of the propagation and the rotation of the liquid/gas interface controlled by a nonuniform and evolving evaporation flux and also evolving contact angles.

The key feature of the tests is that they are made on very long cylindrical grains. That results in the menisci having only one nonzero curvature, and in turn, allows one to directly assess the Laplace pressure, at least at the central part of the cylinders. The direct relevance of the tests is to the behavior of capillary liquid between elongated grains of soils, or fibers, or microcables.

2. Materials and Methods

2.1. Background

To follow experimentally the air entry during evaporation into a 3-or more-grain capillary body is not a trivial enterprise for a 3-D arrangement. In particular, to capture the image of the "internal" (positive) curvature of a 3-D meniscus was considered not possible by direct photography. Mielniczuk et al. (2021) attempted to simulate the process step by step by a computed tomography (CT) imaging of the stills of the water body configurations corresponding to the prescribed water volumes. The resulting morphology and Laplace pressures are approximate, as the evaporation rate effect is lost. Clearly, it is neither possible to capture the unstable parts of the process, occurring within 1/20,000 s.

Prompted by the inability to monitor in real time the internal (positive) curvature of the meniscus for three or more-spherical grain assemblies, we have opted for experiments on long cylindrical bodies of water spanning three glass or PTFE cylinders. The advantage of using long cylindrical grains is in the fact that one of the curvatures of the critical meniscus at the mid-symmetry plane of the water body is zero or near zero, Figure 1b. That means that the Laplace pressure can be calculated based on one curvature, only. This is exactly true for a major

19447973, 2022, 9, Downloaded from https://agupubs.onlinelibrary.wiley.com/doi/10.1029/2022WR031938 by Office Of Scientific And Technical Information, Wiley Online Library on [29/08/2023]. See the Terms and Conditions (https://onlinelibrary.wiley.com/terms-and-conditions) on Wiley Online Library for rules of use; OA articles are governed by the applicable Creative Commons License

19447973, 2022, 9, Downloaded from https://agupubs.onlinelibrary.wiley.com/doi/10.1029/2022WR031938 by Office Of Scientific And Technical Information, Wiley Online Library on [29/08/2023]. See the Terms and Conditions (https://onlinelibrary.wiley.com/terms-and-conditions) on Wiley Online Library for rules of use; OA articles are governed by the applicable Creative Commons License

part of the process. But as evaporation in reality shortens the cylindrical water bridge length, the midplane positive curvature eventually starts growing and may start playing some role. However, as documented in what follows, the ratio of the spans, over which the principal meniscus curvatures develop, varies between 16.97 at the start, to 3 at the instability onset and ends near 1. Hence, at the critical moment at the onset of the first instability, the longitudinal curvature role is still insignificant.

The purpose of the analysis of the collected data is to attempt to deduce, on the basis of the experimental results, the evolution of the morphology of the capillary water body during drying. Special attention is given to components of the mechanisms of an unstable transition between the evaporation rate-controlled portion of the process and the onset of an unstable and dynamic reconfiguration of the water body geometry. For that reason, we follow the images of the right-hand side (RHS) and the left-hand side (LHS) menisci every 10 seconds. We focus on the change in the shape of menisci during the jumps. Additionally, we digitize the propagation of characteristic points of the menisci, that is, the triple contact points and the meniscus midpoint. Furthermore, we follow the change in value of the contact angles.

The changes in morphology of the water body induce an ensuing continuous reconfiguration of the acting forces, that is, Laplace pressure, resultant surface tension forces, weight, as well as resulting d'Alembert forces, activating the Haines jump. The dynamic aspects of Haines jumps are discussed by Hueckel et al. (2022).

2.2. Experimental Setup

The apparatus is conceived to image the front view and side view of a cylindrical 3-grain capillary bridge, as well as to measure the total capillary force. A global view of the apparatus is presented in Figure 1a, accompanied by a schematic view of the examined sample (Figure 1b). The experimental setup consists of a sample mounting and positioning system, two digital photo cameras, and a LED telecentric and analytical scale. The apparatus is installed inside a climate chamber, where relative humidity and temperature are controlled and stabilized (RH = 35% and T = 22°C).

The sample mounting and positioning system allows one to control the vertical separation and alignment between the upper and lower grains. The lower grains are installed on a support, attached to the scale weighting plate, in a fixed position. The upper grain is attached to the upper support and XYZ micrometer stage, which allows to control the separation and the alignment between the two sets of grains (X-Y axis). By design, there is no direct contact between the upper grain(s) and the scale. The experimental setup has been described previously by Mielniczuk, Hueckel, and El Youssoufi (2014).

There are two main geometrical variables that affect water body behavior in capillary conditions: meniscus curvature and contact angle. Under a set of assumptions, they lead to two crucial dynamic capillary variables, that is, Laplace pressure (or the difference between the pressure on both sides of the liquid/gas interface) and the line force of surface tension acting on the interface line between three phases involved: liquid/gas/solid. By Young-Laplace law (Laplace, 1805 and Young, 1805), Laplace pressure is proportional to the average of the two principal curvatures of the interface between the liquid and the gas phase. It acts orthogonally on the above mentioned interface and on the solid grain across the surface area of solid/liquid contact. The surface tension force acts along the tangent to the liquid surface at its triple interphase contact line. And it evolves with the contact angle. The force itself is articulated per unit length of the perimeter. The pressure resultant and the surface tension force resultant produce an adhesion force of the capillary liquid to the solid grain. In the context of a grain cluster, it constitutes its capillary cohesion (see e.g., Fisher, 1926 and Hueckel et al., 2020).

In the experiments, the capillary bridge between the two sets of grains is created by injecting a prescribed amount of deionized distilled water (following an established protocol) with a laboratory syringe. At the moment of injection of water, the apparent weight reading on the scale changes (decreases) because of the creation of an intergranular attractive (capillary adhesion) force between the grains, transmitted by the liquid bridge. During evaporation of the liquid, the intergranular force (apparent weight) changes.

The grains that were used are either made of borosilicate glass or polytetrafluorethylene (PTFE). The grain diameters and length of the cylinders are, respectively 3.96 and 8.57 mm for glass and 3.23 and 8 mm for PTFE. The vertical separations of grains (as defined in Figure 2b) are from 327 to 1,239 μm, for glass cylinders and from 327 to 1,486 μm for PTFE cylinders. The initial water volume was 10 μl for both types of grains. In this paper,

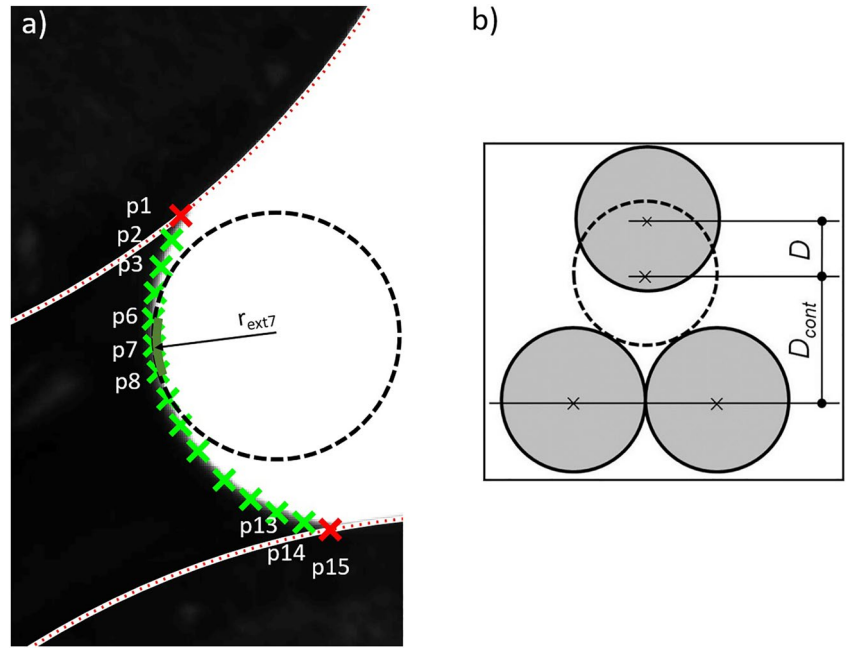

Figure 2. (a): Virtual points, marked on bridge meniscus profile (p1–p15), with an example of the determination of the external radius for point p7, using a segment of the meniscus profile from points p6 to p8; (b) definition of the grain row distance, D.

we report only the results for the glass cylinders with a separation of 434 μm. A parametric study with a different solid material and at different separations is presented elsewhere.

Two digital photo cameras are recording an evolution of bridge profiles from two different points of view: one camera is pointing at the front of the bridge aligned with the cylinder axes, while the second camera allows to observe the side. Using LED telecentric backlight, it is possible to enhance the visualization of the edges of grains and the profile of the capillary bridge.

The intergranular force evolution and sequences of photos obtained from two cameras are recorded continuously during the process, every 2 seconds for the intergranular force and every 10 s for the photo cameras.

For each test, the obtained data consist of two sets of image sequences (front and side view) and the measured intergranular force evolution as a function of time. Parallel tests were conducted in order to measure evaporation (total water mass evolution) in time. During these tests, the entire sample is sitting on the scale, what allows us to measure the weight decrease in time.

Based on geometrical parameters determined for the front and side views of the capillary bridge, it is possible to determine four contact angles, using a linear approximation of the bridge tips and grain dimensions. The exact actual vertical distance between the cylinders is also calculated. Description of the procedures adopted to digitalize the evolution of the meniscus profiles is provided in Appendix 1, whereas the raw data and software employed to process them are available at https://osf.io/e465m/

The procedure allows us also to determine the moment of passage of the bridge profile (contact points or middle point) through the throat, where the distance between grains is the smallest. The displacement, velocity and acceleration of bridge profiles may be determined, with reference to the points initial profile position of the meniscus using measured coordinates of virtual points marked on the bridge profile. An average curvature of the bridge profile in the middle point has been determined using the data of the central 1/5th of the overall profile length. Changes of the curvature in time (velocity and acceleration) are also determined, see Hueckel et al. (2022).

19447973, 2022, 9, Downloaded from https://agupubs.onlinelibrary.wiley.com/doi/10.1029/2022WR031938 by Office Of Scientific And Technical Information, Wiley Online Library on [29/08/2023]. See the Terms and Conditions (https://onlinelibrary.wiley.com/terms-and-conditions) on Wiley Online Library for rules of use; OA articles are governed by the applicable Creative Commons License

19447973, 2022, 9, Downloaded from https://agupubs.onlinelibrary.wiley.com/doi/10.1029/2022WR031938 by Office Of Scientific And Technical Information, Wiley Online Library on [29/08/2023]. See the Terms and Conditions (https://onlinelibrary.wiley.com/terms-and-conditions) on Wiley Online Library for rules of use; OA articles are governed by the applicable Creative Commons License

3. Data, Findings and Their Context

The database collected during evaporation experiments and presented here are data regarding evolution of the water bridge between three glass cylinders at an intermediate separation of 434 μm. Separation is defined as in Section 3, Figure 2b. The results presented here concern morphology and kinematics of the capillary water body during drying. The discussion of dynamics, instabilities, and post-critical behavior of the capillary water body is provided in the companion paper, Hueckel et al. (2022).

The separation of 434 μm, or nondimensionally of 0.11, if related to the grain diameter, places it in the midrange of separations, sufficiently large to ensure instability of the lateral (negative Gauss curvature, GC) meniscus, as opposed to the double-bowl, positive GC instability, and sufficiently small to induce a highly energetic (dynamic) air entry (see Mielniczuk et al., 2021).

It should be underlined that there are several modes of surface instabilities of capillary bodies, dependent on grain configuration, inter-granular distances (or/and porosity), grain solid/fluid contact angle (Hueckel et al., 2020; Mielniczuk, El Youssoufi, et al., 2014; Mielniczuk et al., 2015, 2021). This paper presents the results of experiments generating finger-type Haines jumps.

The database also includes (not published here) data for the capillary bridges for glass cylinders at other separations, as well as, a subset database of capillary bridges for 3 PTFE cylinders at various separations. The effects of the grain material and separation on the air entry onset and development are discussed elsewhere.

3.1. Capillary Water Body Morphology

The morphology of evaporating capillary bridges changes in a nonuniform but consistent way. In what follows, we list the main characteristics of such changes.

1. For separation of 434 μm, the entire initial mass (of 10 μl) evaporates within ab. 4,400 seconds (73 min). As in many other drying processes, the global mass loss rate is nearly constant, slightly decreasing in time, Figure 3a. There are two types of intercalating processes during drying: one, a slow water boundary retreat, seemingly controlled by the evaporation rate, and other, fast one, during which the body of water undergoes (twice in this case) a complete dynamic reconfiguration but without any visible relationship to evaporation nor evaporation rate. These processes were termed by Melrose (1970) as isons and rheons, respectively, see also Morrow (1970).

2. The bridge initially is nearly symmetric and evolves symmetrically for the first 1,000 s (Figure 3b), while after about 1600s the Right-Hand Side (RHS) meniscus starts accelerating, whereas the Left-Hand Side (LHS) meniscus remains much slower. That takes place at the cluster saturation equal to 0.572, hence roughly at less than half of water being evaporated. LHS meniscus then decelerates around 1900th s and eventually practically stops moving at about 2000th s, which is curious, as it is evaporating at the presumably constant rate. Because of an increasing displacement of the RHS contact point, at the practically immobilized LHS contact, the symmetry of the bridge is visibly lost, and the liquid/solid contact surface of the top grain becomes tilted, as shown for 2,020 s in Figure 3c. At 2,070 s. the RHS meniscus acceleration becomes beyond measurable and within the next two snapshots, the RHS meniscus exhibits a jump forward (2,070–2,090 s), see Figures 3d and 3e. That happens at the meniscus position at what is referred to as a throat point between the top grain and the bottom RHS grain (i.e., the spot of the closest distance between the two grain surfaces). Simultaneously, at 2,070 s, the LHS meniscus produces a backward jump of a smaller distance and then remains practically immobile until the 2600th s. The RHS jump is recognized as the Haines jump (Haines, 1928) or air entry (Morrow, 1970 and Melrose, 1970).

After 2100s, the RHS meniscus substantially decelerates, and its further advancement returns to the previous rates. It progresses at that rate until around 2,310 s. At this point the RHS meniscus approaches the surface of the LHS bottom grain. At the instant of contact, the RHS meniscus splits into two separate menisci: one between the top and left bottom grain and another one between the two bottom grains, Figure 3f. The new RHS meniscus solid contact point splits subsequently between the RHS meniscus lower contact point and what becomes a left contact point of the new bottom meniscus, which effectively evolves from a lower part of the RHS meniscus, while its RHS contact evolves from the bottom contact point of the RHS meniscus. Thus, the RHS meniscus undergoes an apparent jump of its bottom contact, over a distance of nearly ¾ mm, but its kinematics in reality is more complex.

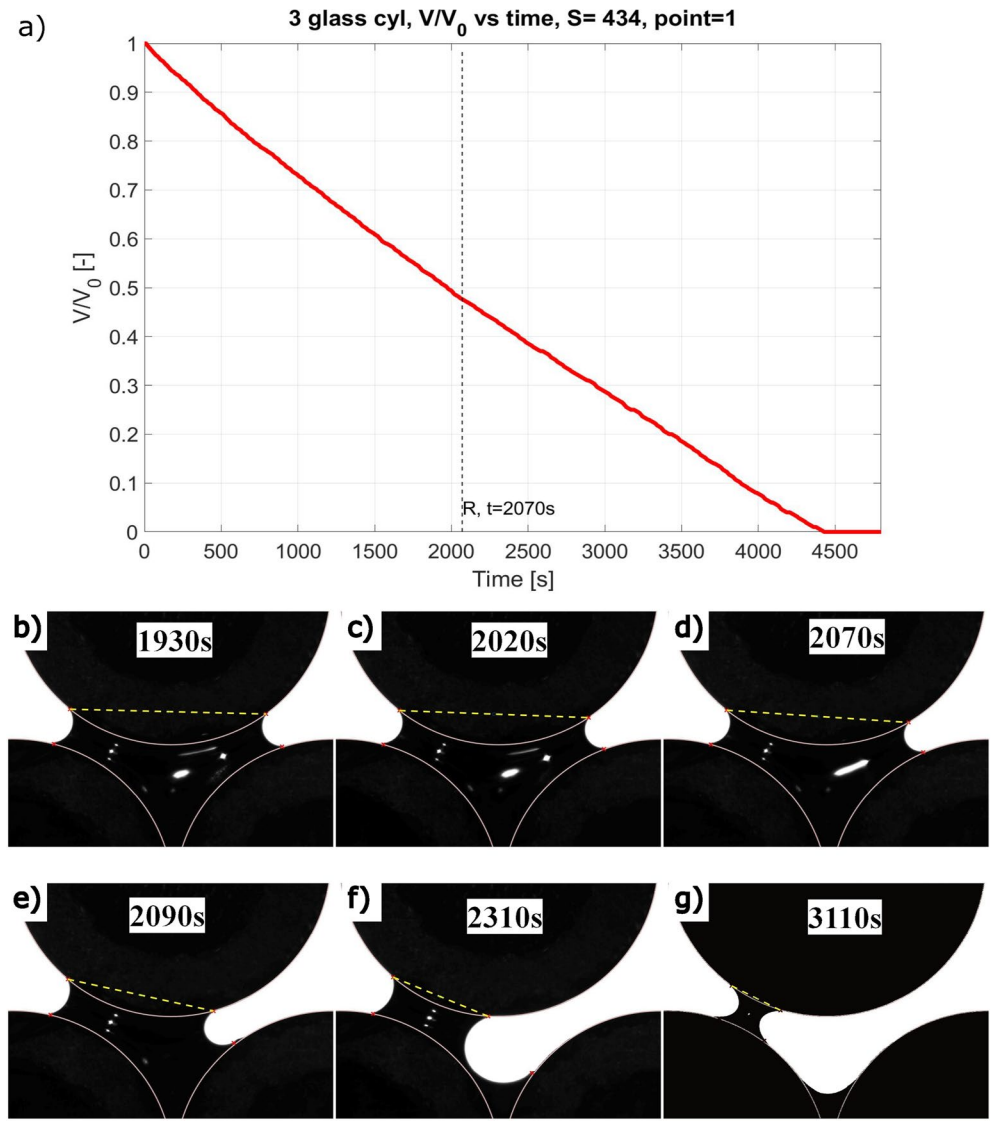

Figure 3. (a) Relative water volume change as a function of time; Snapshot images of the lateral view of the capillary bridge. (b–e): late symmetric stage: note the increasing tilting of the upper liquid/solid contact, ending with a jump between 2070 and 2090s, after which (f) and (g) a nonsymmetric stage starts.

The RHS meniscus split divides the original single water body into two separate bodies, Figure 3f. One becomes a pendular bridge between the top grain and the bottom left grain, and the other one, substantially smaller, is symmetrically wedged between the two bottom cylinders in contact, Figure 3g. The latter one evaporates fast with a meniscus sinking down the central well, and without contributing to the contact with the top grain. The LHS pendular bridge shrinks steadily and nearly symmetrically, until it ruptures around 3110s, with a considerable liquid water mass. No particular form of its rupture or vanishing has been observed. A study of the rupture of pendular bridges between spherical glass grains identifies four subsequent instabilities of different nature (Mielniczuk, El Youssoufi, et al., 2014; Mielniczuk et al., 2015 and Zhao et al., 2020).

3. The images of individual menisci on both sides of the water body were acquired photographically every 10 seconds and contoured from the identified triple contact points while using the other (13) points of the interface, employing an in-house developed procedure of computerized contouring of a midplane cross-section. The contours of the menisci are presented in Figures 4a and 4b. More than 320 profiles were recorded all together. As it is clear from the figures, the progress of the menisci through the landscape of grain arrangement is characterized not only by a variation in their motion rates but also by modification of the meniscus length, depth,

19447973, 2022, 9, Downloaded from https://agupubs.onlinelibrary.wiley.com/doi/10.1029/2022WR031938 by Office Of Scientific And Technical Information, Wiley Online Library on [29/08/2023]. See the Terms and Conditions (https://onlinelibrary.wiley.com/terms-and-conditions) on Wiley Online Library for rules of use; OA articles are governed by the applicable Creative Commons License

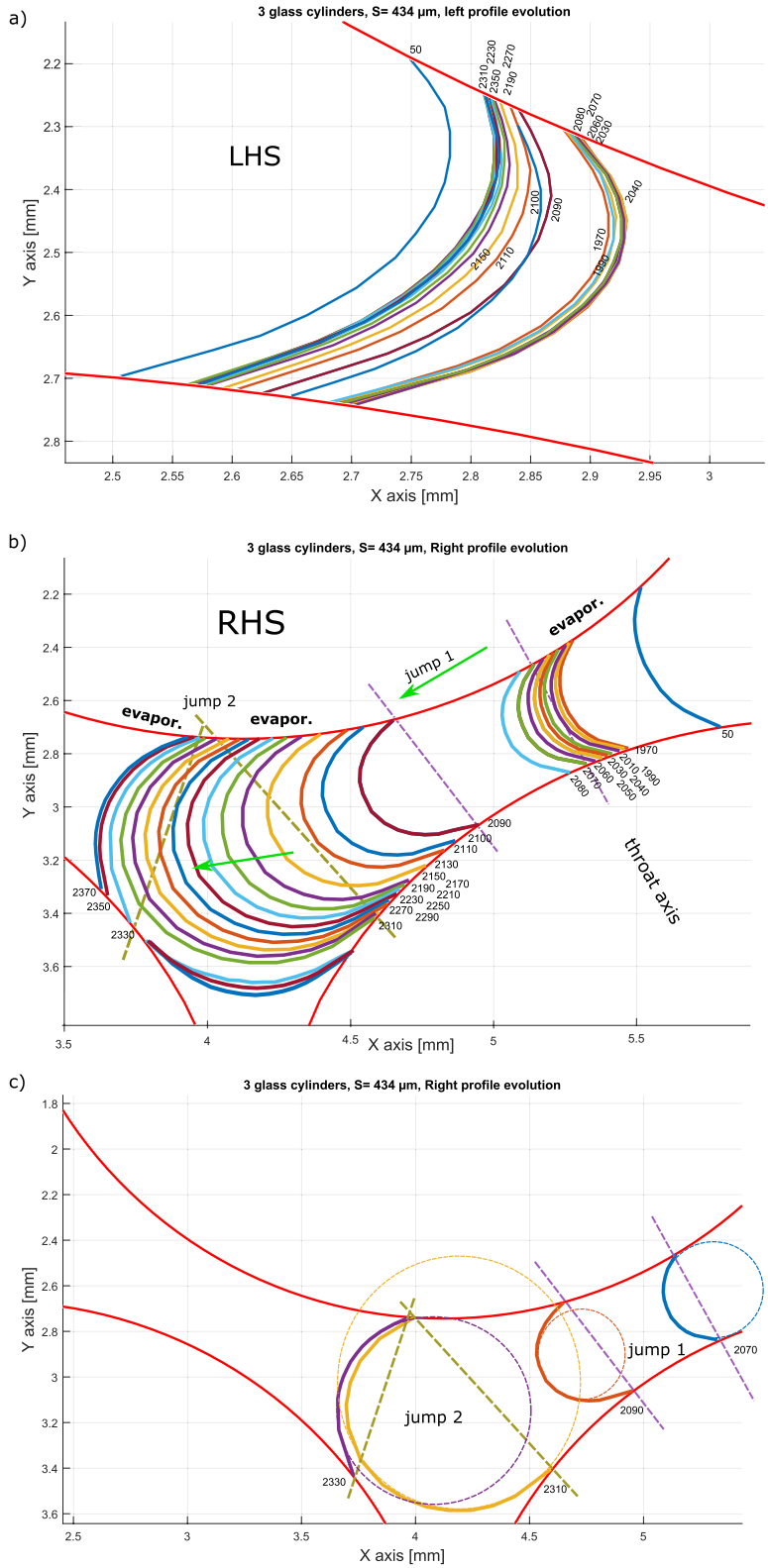

Figure 4. Evolution of menisci at the left-hand side (a) and right-hand side (RHS) (b) liquid/air interface of a bridge of three cylindrical glass grains at a nominal separation of 434 µm. The blue-dashed line is placed at the Throat (of the shortest distance between the grain edges; (c) RHS menisci at the start and the end of Jump 1 and Jump 2.

19447973, 2022, 9, Downloaded from https://agupubs.onlinelibrary.wiley.com/doi/10.1029/2022WR031938 by Office Of Scientific And Technical Information, Wiley Online Library on [29/08/2023]. See the Terms and Conditions (https://onlinelibrary.wiley.com/terms-and-conditions) on Wiley Online Library for rules of use; OA articles are governed by the applicable Creative Commons License

19447973, 2022, 9, Downloaded from https://agupubs.onlinelibrary.wiley.com/doi/10.1029/2022WR031938 by Office Of Scientific And Technical Information, Wiley Online Library on [29/08/2023]. See the Terms and Conditions (https://onlinelibrary.wiley.com/terms-and-conditions) on Wiley Online Library for rules of use; OA articles are governed by the applicable Creative Commons License

shape, and most importantly, curvature. As the "other" (longitudinal) curvature is nearly zero, by Laplace law. Figures 4a and 4b imply, among other things, a nonuniformity of the resulting Laplace pressure and, presumably, water flow within the bridge, both during the "jump phase" as well as during the earlier "evaporation dominated" phase. However, the internal capillary water flow was not measured and thus is not considered in what follows.

4. To visualize the extent of evolution of the meniscus, its size, form, and orientation for the RHS are exemplified for selected instances in Figure 4c. The depth of the meniscus evolves from about 150 μm initially, to about 220 μm at the first jump's start and 380 μm, when it ends, and becomes about 510 μm when the original meniscus splits (i.e., at the second jump). The first jump amounts to about 700 μm, measured at the meniscus tip. The meniscus, in brief, as being first transitioned by the progressing evaporation into a tighter space, undergoes a shortening and deepening. After passing the throat, the meniscus enters into a widening space, undergoing an extension but also a deepening and a rotation. As it is clear, the evolution is constrained by the geometry of the space available, that is, several elements of the configuration, in particular the distance between the solid boundaries, the change of the orientation of the former ones at the points of contact, and induced by the propagation of the liquid/gas interface imposed by the process of evaporation.

5. In general terms, we note that one of the principal postulates of the Young-Laplace (Y-L) concepts of a capillary interface, which is that its mean principal radius of curvature is constant (see Laplace, 1805; Young, 1805), is not verified for the observed menisci. There are a few possible explanations for the observation. First, for the menisci for long cylindrical grains, idealized as (2-D) surfaces, that is, with their longitudinal curvature practically zero (see Figure x in the Supporting Information S1), the Y-L postulate implies that any static meniscus cross section perpendicular to the bridge axis is a circle. However, the Y-L equation is established for a capillary interface between two static fluids. Hence, for the considered case of a moving interface activated by evaporation, as well as for a capillary bridge extension or contraction, fluid motion is expected, as is a departure from the meniscus circular shape. For the imaged photos identified with the profiles of cross sections at the center of the bridge, the curvature radius at the midsection is consistently lower than near the contact, Figure 4c (see also Hueckel et al., 2022). The latter is related to the contact angle, which is visibly variable. It is to be underlined that across the meniscus surface there is a water flux due to evaporation, which is not expected to be uniform (Yang et al., 2018, see also Hu & Larson, 2005). For further discussion of the subject, see Hueckel et al. (2022).

Especially evident are the meniscus changes occurring immediately prior to and during the jump, both at RHS and LHS, between 2,070 s and 2,090 s, related to the meniscus transitioning through the throat. The mean radius passed through the RHS throat is smaller than its counterpart at the throat, despite that the distance between the contacts being larger. The apparent, second jump between 2,310 and 2,330 s involves an evolution of a nearly spiral (logarithmic) into two separate menisci with two new contact points of the split interfaces, Figure 4c. Detailed analysis of curvatures is presented in the companion paper, Hueckel et al. (2022).

From the fluid dynamics point of view, it is realized that the evolution of the water body responds to the above stimuli while maintaining the continuity and equilibrium, when possible, the physics of the flow, the constraints of the moving and a priori unknown interface, and boundary conditions. The latter two are viewed by many as open issues of complicated physics depending on the scale at which it is considered, see for example, Scardovelli & Zaleski, 1999. Some of the elements of the whole multiphysics process have been observed, but not measured, some have been measured at selected points, still some have been calculated, based on a set of assumptions, as presented below and in the companion paper.

3.2. Kinematics

The described changes in morphology of the capillary water body during evaporation can be represented by several variables that capture numerically their main characteristics. Via known constitutive laws of capillarity, it is then possible by following their trends and correlations to recover the evolution of the related physical variables and establish relationships between them.

1. The most visible and directly measurable kinematic variables are those describing the propagation of the meniscus, especially of the displacement of the points of triple contact between liquid/solid/gas phases. These contacts form lines along the generatrices of the cylinders (two, on both sides of the top cylinder, and one for each of the bottom cylinders. The bottom cylinders are in solid-solid contact laterally (and a meniscus between

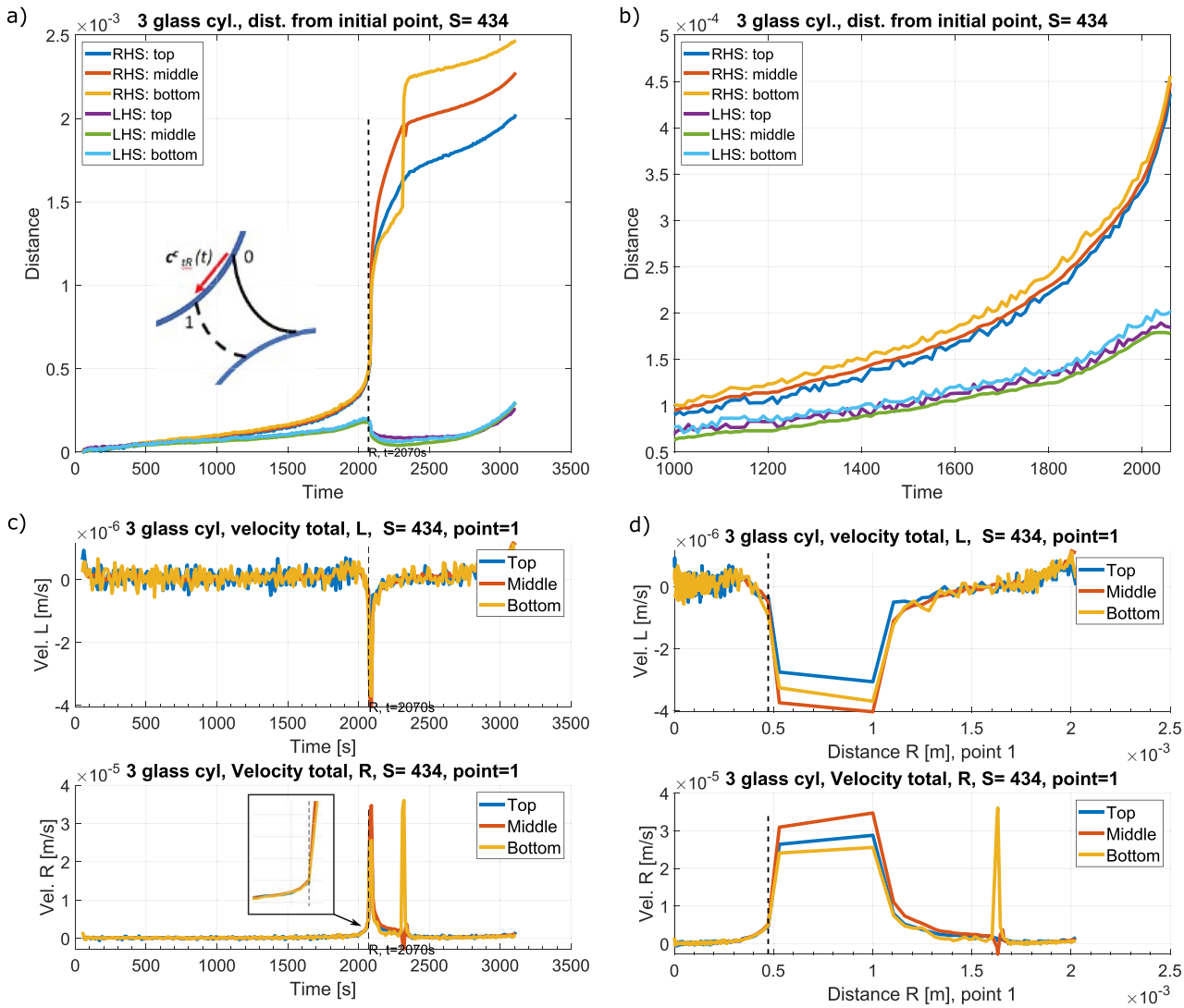

Figure 5. (a) Distance (positive when oriented toward bridge center) from the initial position of the right-hand side (RHS) and left-hand side (LHS) top and bottom triple (liquid/gas/solid) contacts, as well as midmeniscus points as a function of time. The inset shows the variable of distance of RHS top contact from its original location. The vertical line in the middle shows the moment when the RHS top contact point passes through the point of throat between the top grain and the RHS bottom grain. A clear acceleration of the RHS meniscus is seen starting from 1890 s, becoming uncontrolled at 2,070s; (b) A blowup of early stage of the evaporation driven process showing forth and back displacements of the contacts, which after 1,780 s gradually cease to jerk back on the RHS while substantially increasing the steps forward; Velocity from the initial position of the top and bottom contact points as well as of the midpoint of the RHS and LHS menisci, respectively, versus time (c) and versus the position of the RHS meniscus top contact displacement (d). Note that while the velocities at the LHS are positive at the beginning they turn to negative, when the RHS undergoes the 1st Jump.

them, when formed, evaporates practically instantly). In the images of the front view and at their cross-section with the bridge midplane, these lines are represented as points. These are not material points, but moving loci in space where the three phases meet. The distance from its original position at the RHS, denoted c^c_{tR}, is shown in Figure 5a. Propagation for the RHS and LHS top and bottom triple points is shown in Figure 5b, together with the distance for the midpoint versus time. The midpoints are defined at a position of the bottom of the 7th/15 equal segments of the current meniscus (of a variable length). The distance is positive when oriented toward the center of the bridge.

It is seen that the menisci re-morph with a variable rate and singularities. In the early phase, 0–1,500 s, the contact points and the midpoint travel together, while their propagation rate grows from 0.5 to 2×10^{-4} mm/s. Prior to and during the first meniscus jump at 2070s and the subsequent deceleration phase, the RHS midpoint advances

19447973, 2022, 9, Downloaded from https://agupubs.onlinelibrary.wiley.com/doi/10.1029/2022WR031938 by Office Of Scientific And Technical Information, Wiley Online Library on [29/08/2023]. See the Terms and Conditions (https://onlinelibrary.wiley.com/terms-and-conditions) on Wiley Online Library for rules of use; OA articles are governed by the applicable Creative Commons License

19447973, 2022, 9, Downloaded from https://agupubs.onlinelibrary.wiley.com/doi/10.1029/2022WR031938 by Office Of Scientific And Technical Information, Wiley Online Library on [29/08/2023]. See the Terms and Conditions (https://onlinelibrary.wiley.com/terms-and-conditions) on Wiley Online Library for rules of use; OA articles are governed by the applicable Creative Commons License

the most, and the bottom contact the least, coming to a standstill at about 2,300 s. The velocity for the midpoint grows from 0.1×10^{-3} mm/s to 1×10^{-1} mm/s, and returns back to 2.25×10^{-3} mm/s, respectively. The second meniscus jump, at 2,310 s consists primarily of a split of the RHS meniscus, when the latter comes in contact with the LHS solid grain perimeter. That results in a switch of the RHS bottom contact to the LHS bottom cylinder, while the top and midpoints remain practically immobile. Hence, the jump refers to the bottom contact point of RHS meniscus, only.

Also notable is that the original LHS meniscus also undergoes a jump, but consisting in a reversal of the original motion, and which is of about -0.15×10^{-3}m, that is 10 times smaller than that on the RHS.

It needs to be emphasized that velocities shown during the jump are not the actual values, as they refer to the intervals of 10 s at which images are taken. In reality, the motion during the jump is orders of magnitude faster and would require a high-speed camera to be captured. An assessment of the jump duration can be obtained from the momentum balance associated with the jump (see Hueckel et al., 2022). Similarly, the kinematics of the meniscus split is not captured in detail, but it is not associated with any water mass displacement.

Initially, the left and right top contacts retreat toward the bridge center at a similar (constant) rate, commensurable with the evaporation rate. The RHS triple point (velocity is positive from R to L) starts to advance visibly faster than its LHS counterpart (velocity is positive from L to R), at the time around 1200s. At 1600s the RHS translation is 50% larger than that at LHS. After 1,900 s the RHS accelerates almost instantly, while the LHS contact to the contrary, starts decelerating around 2000s, and about 2040s the LHS meniscus starts going back, however nearly 10 times slower than its RHS counterpart. At 2,070 s. figuratively speaking, the RHS meniscus instantly pushes to the left the entire water volume, including its LHS meniscus. That is a short-lived but very consequential event. It lasts less than 20 s. The LHS meniscus eventually stops moving at 2,080s. When it re-starts moving again around 2,500s, it changes its sense once more. After 2,090s, both menisci retreat again controlled by the evaporation rate, for some time. For reference, the vertical dotted line in the middle of Figure 5 shows the moment (2,070 s) when the top RHS meniscus point passes through the point of throat. Notably, on both sides, the two contact points and a meniscus midpoint propagate with the same rate, until about 50 μm before the instant when the RHS contact reaches the point of throat at about 2,070 s, when an instability takes place. During the instability, the RHS meniscus reconfigures, with the midpoint by far leading the jump (the rate is twice as big in the midpoint than at the contacts) with the contacts lagging. This is also seen as the meniscus sharpening between 2,070 and 2,090 s, see Figures 4b and 4c. That leads to a substantial increase in the curvature at the midpoint (see the companion paper, Hueckel et al., 2022).

3. Lengthwise, the RHS meniscus jump amounts to about 650 μm, as best seen in Figure 5c, but occurs within 20 s and involves a dramatic spike of the velocity. This is followed by an immediate deceleration back to the previous velocity values. In rough terms, the first jump moves the meniscus by a distance equal to nearly twice as much as the total propagation at the jump onset. In other terms, the Haines jump amounts to nearly twice the evaporative meniscus propagation, in terms of length.

After the first jump is completed, as evaporation proceeds at the regular rate, so does the meniscus propagation, until the right cylinder contact points slow down (especially the bottom contact), compared to the midpoint. At a configuration, in which a RHS meniscus point comes into contact with the LHS cylinder, a second re-configuration occurs, which may be viewed as a meniscus split. The location of the point of split as an RHS meniscus is related to the shape of the meniscus prior to the split. The shape of the meniscus departs largely from the circular one, postulated by the Laplace law, and resembles one of a (logarithmic) spiral. The velocity of translation of the top meniscus contact point (shown in Figure 5d) does not exhibit any singularity, as opposed to the 1st jump. The kinematics involves just a spike for the bottom contact switching from one grain to another, dragging behind the midpoint, but marginally. The very nature of the second jump is different, as it consists of a breakdown of the large RHS meniscus into two separate menisci at the spot of new air/solid contact. The first new meniscus forms now the RHS boundary for a LHS pendular capillary bridge, and the second meniscus develops between the two bottom grains. However, the bottom meniscus disappears within about 200 s, converting into thin liquid films attached to the bottom grains. The second jump does not involve the top grain and the RHS top contact, and produces no jump in the capillary adhesive force, as can be seen in Hueckel et al. (2020).

It may be concluded that two-third of the progress of the meniscus occurs via micro-pulses of the first Haines jumps. It is expected that the same applies to the drying front which appears to be a macroscopic representation

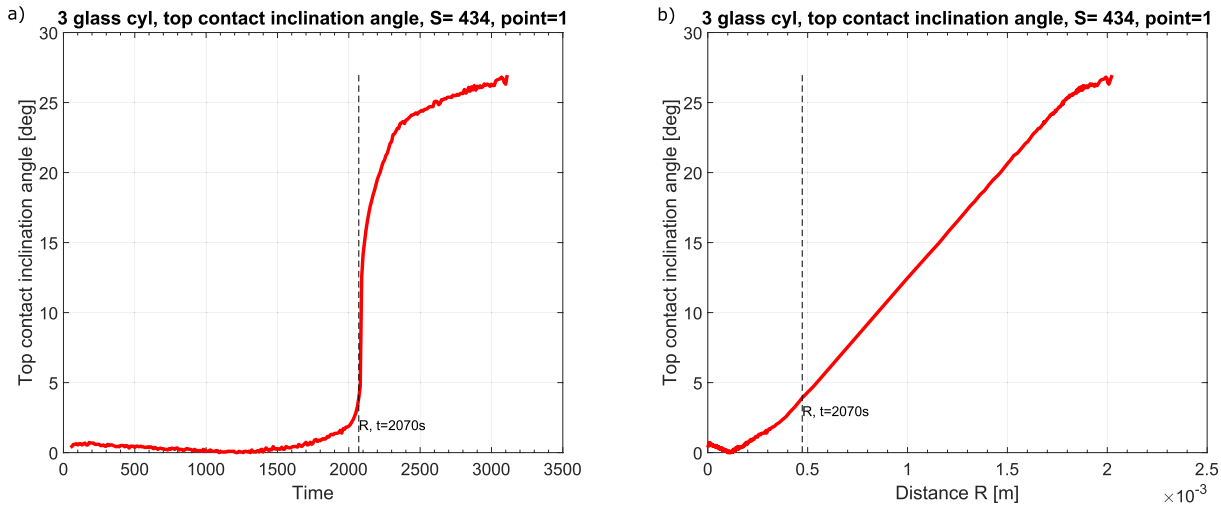

Figure 6. The rotation of the liquid/solid contact surface for the top grain, shown in terms of the inclination angle between the imaginary plane of L/S contact (or between the two triple contact points) and the horizontal plane (a) versus time and (b) versus distance of the top right-hand side triple point from its original position.

of a chain of menisci. As for the second jump, it is a bit more complicated. Quantifying it by the bottom contact progress, it is one-third the steady evaporation and two-third the jump, as far as distances are concerned. From the point of view of reconfiguration of the water body, the second jumps produce the pendular bridges (see Hueckel et al., 2020; Mielniczuk et al., 2021). Thus, less than half of the progress of the drying front occurs as a result, and with the rate, of evaporation, while more than half of the progress consists of the jumps, with the rate several orders of magnitude higher (see Berg et al., 2013).

2. The visibly growing initial disparity of the motion of the two menisci on the two sides leads to a gradual rotation of the liquid/solid (L/S) contact surface for the top grain. Approximating the contact surface as a plane, the rotation may be measured by its inclination angle change. The evolution of the angle of the L/S top contact is shown in Figures 6a and 6b. The contact starts rotating relatively early, that is, at about 1,400 s, which is a 1/4th of the time of reaching the throat, and reaches about 5°. Within the next 20 s, it reaches 15°, and starts slowing down at 25° at about 2,600 s. The L/S contact starts tilting when the RHS meniscus is 0.75 mm ahead of the throat and stops tilting when the meniscus passes the throat. The tilt is very important as it induces a horizontal component to the adhesive force within the system.

The acceleration of the meniscus motion arises when the contact points come near the throat at the time shortly before 2,070 s. Notably, at that point, half of the initial water body is already evaporated and the system geometry is visibly altered. However, once the RHS meniscus passes the throat point, the water body develops a very high acceleration, but for a rather short time.

4. Figures 5b and 5c put the above observations into a larger perspective of the kinematics of the ***lower*** contact points of both menisci, as well as that of the midpoints of both menisci. First, during the symmetric phase of the process, the motion of all three points of menisci, both at RHS and LHS, is practically the same. Second, the figures emphasize the fact that from the point at which the bridge symmetry is lost, up to the end of the process, the displacement of RHS meniscus grows over one order of magnitude larger, compared to that of the LHS, for practically all the meniscus points. That is not the case anymore in the post-critical phase, when the top contact is the least advanced on the RHS while the most advanced is the lower contact. Conversely, at LHS, during the bump-back phase, the midpoint retracts the most and the top contact the least, while during the final phase of advancement (which is a pendular phase), all three points advance uniformly again.

5. One major conclusion from these observations is that the shape of the menisci evolves, which implies that the curvatures (and hence, pressures) are unlikely to be constant across the meniscus. This in turn implies the likelihood of the fluid flow, not only during the instability episodes, but also during stable steady, evaporation-controlled meniscus propagation. A similar conclusion was derived from the pendular bridge analyses by Yang et al. (2018). Figure 5 shows that the meniscus midpoint advances much faster (with a difference of the order of 2–3 times)

19447973, 2022, 9, Downloaded from https://agupubs.onlinelibrary.wiley.com/doi/10.1029/2022WR031938 by Office Of Scientific And Technical Information, Wiley Online Library on [29/08/2023]. See the Terms and Conditions (https://onlinelibrary.wiley.com/terms-and-conditions) on Wiley Online Library for rules of use; OA articles are governed by the applicable Creative Commons License

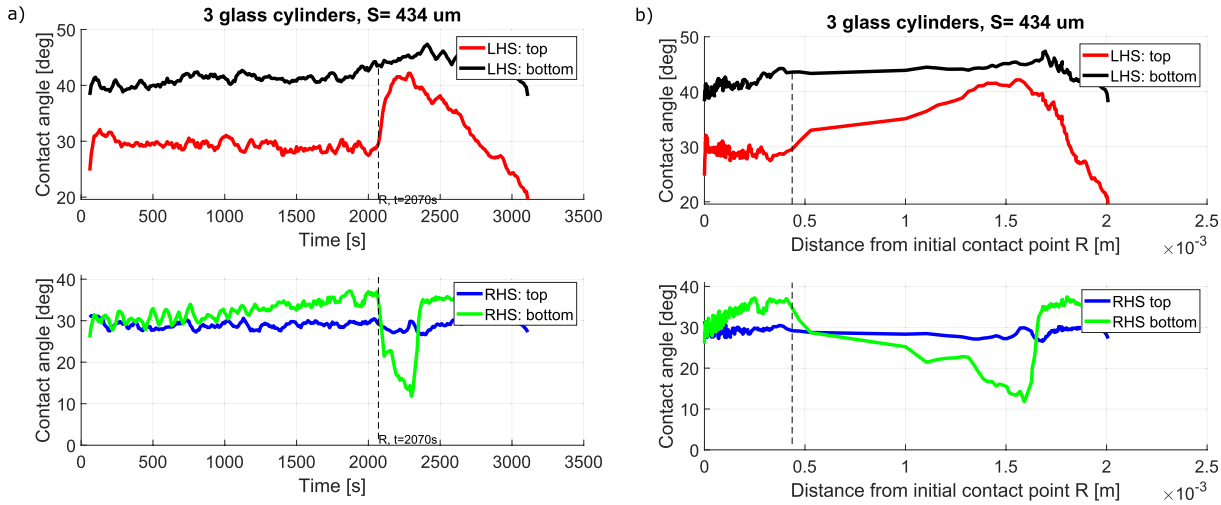

Figure 7. The rotation of the liquid/solid/gas contact angle for: (a) left-hand side (LHS) and right-hand side (RHS) meniscus at the top and bottom grain contact versus time (b) LHS and RHS meniscus at the top and bottom grain contact versus distance of the RHS top contact from its initial position.

than the top and much more with respect to the slowest, bottom contact point). That obviously implies that the meniscus depth becomes larger.

It is noticed that the peripheral segments of the RHS meniscus (top and bottom) are controlled by the contact angles that remain relatively unchanged. The evolution of the top and bottom RHS and LHS contact angles is reported in Figures 7a and 7b. The top contact angles on both sides remain practically the same (apart from the stick and slip harmonics) until the top RHS contact approaches the point of the throat. The bottom contact angles, instead, gradually increase, initially with a very similar rate on both sides. The total increase is not large, from 30° to 37° (RHS) and from 40° to 43.5° (LHS), but consistent. At the point of throat, the bottom RHS and the top LHS contact angle undergo jumps upon the reconfiguration of the bridge. But the details of their dynamics are different. The RHS bottom contact, when reaching the throat, rotates by 15° instantly, as the contact jumps about 0.1 mm ahead, and by another 10° within 100 s of the slightly slower displacement. This change is likely to be the most significant geometrical change in the entire meniscus.

However, the bottom contact is completely reconfigured within the next 100 s during its second jump between the RHS and LHS bottom grains, as it splits into two, as described above. The LHS top contact angle reverses its course once the RHS meniscus instability is triggered but only for a moment. Such a complex evolution of the contact angles is to be seen in the context not only of the changing geometry of the boundaries, but also of the reversal of the sense of the motion of the LHS meniscus contact from advancing to receding and back to advancing. That type of behavior was found to play a critical role in the mechanics of drying, as seen for sessile droplets (see Armstrong et al., 2019; Joanny & De Gennes, 1984; van der Heijden et al., 2018).

The role of the contact angle change in the evolution of the resultant surface tension forces needs to be emphasized. In particular, the change of 25° of the bottom RHS contact angle prior and during the instability leads to a significant rotation of the surface tension force there. As a consequence, the decrease in suction force at the throat induces an inertia force to maintain equilibrium. That generates an acceleration of a mass of water, hence producing the first unstable jump of the system. For details of the dynamics, see Hueckel et al. (2022).

6. The meniscus instability just mentioned can be seen as producing a rapid displacement of the water mass from the RHS being pushed out by the dynamically evolving RHS meniscus perpendicularly to the axis of the bridge. The water mass displacement results in the reversal of motion of the LHS meniscus and the water mass near it. However, in the longitudinal direction, the evaporation results in a shortening of the water cylinder. Notably, the RHS instability causes some perturbation in such shortening. During the first phase of the instability, as can be seen in Figures 8a and 8b, there is a slowdown of the shortening, followed by a small and short-lived back-lengthening of the bridge, corresponding to the RHS meniscus jump. Then, there is a subsequent quite substantial very fast shortening. This may be interpreted as the first RHS jump not only pushing water from the RHS into the LHS but also perpendicularly along the longitudinal axis of the bridge. That is followed again by

19447973, 2022, 9, Downloaded from https://agupubs.onlinelibrary.wiley.com/doi/10.1029/2022WR031938 by Office Of Scientific And Technical Information, Wiley Online Library on [29/08/2023]. See the Terms and Conditions (https://onlinelibrary.wiley.com/terms-and-conditions) on Wiley Online Library for rules of use; OA articles are governed by the applicable Creative Commons License

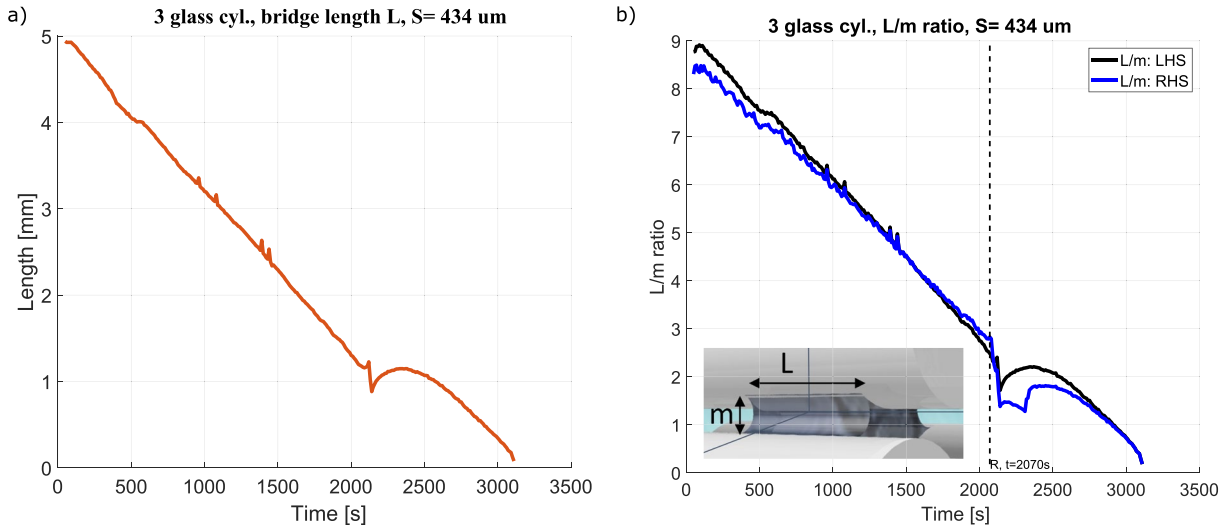

Figure 8. (a) variation of the length of the bridge; (b) a ratio of the spans over which the principal meniscus curvatures develop, L/m, of the length of the bridge, L to the distance between the top and bottom contact points of the menisci, m.

an extension during the second (lower contact) jump and a reversal of almost all the recent length perturbations. As mentioned, the second jump corresponds to the split of the RHS meniscus into two menisci, and eventually a switch from the RHS bottom grain contact to the LHS bottom grain contact, without a substantial water mass motion.

7. Both top and bottom contact points undergo a microrocking or stick-and-slip motion right from the beginning of evaporation, and largely random. This is shown in Figure 5b, which depicts translation of the meniscus points at a smaller scale (10^{-4} m). That implies that the contact points of the cross-section of the cylindrical grain/liquid boundary jump back and forth, independently one from another. As a result of this, a contact point (say, at the top of the meniscus) on one side is for a moment ahead of its counterpart on the other side, but just for a brief moment. As these jumps are random in their quantity and their location along the perimeter, it is very likely that the advancement of one side becomes accidently much larger than the other one, to the point that it prevents a usual snap-back. An example of this can be noticed after the time of 1,800 s on the RHS, where both at the top and bottom contact points, the incremental forward-slips, were until that time followed by roughly half-sized backward-slips, but not anymore. Indeed, the forward-slips increase more than twice, and soon become about 10 times larger than the miniscule backward-slips, which eventually disappear near the time of 2,000s. Most notably, nothing similar happens at LHS, where backward-slips remain unchanged. That generates an onset of acceleration of the motion of the meniscus at RHS. It can be suggested that a precursor for such development, which can also be seen as a microscale cause, is the aforementioned contact tilting, which started around 1,500 s. This is a common behavior analogous to the pinning-depinning occurring at a larger time scale during drying and sliding of droplets as documented by a vast literature (see e.g., Joanny & De Gennes, 1984 and Bormashenko et al., 2011). Widely cited reasons for that behavior include asperities and other microscale defects in the smoothness of the solid surfaces, solid impurities sedimented from the liquid, or caught from the atmosphere.

4. Repeatability

To ensure the representativeness of the discussed results, the experiments were replicated four times. However, the current experimental procedure requires a manual positioning of the grains on a creeping epoxy glue substrate. As a result, minor differences between the actual separation of the grains were observed, as well as some departures from the symmetry of the setup geometry. The recorded separations as defined in Figure 2b were: 397, 393, 573, and 434 μm. Rather than presenting averages of various characteristics of the process from those experiments, we report actual physical values for one single case with separation of 434 μm, as the closest to the mean separation (449 μm).

19447973, 2022, 9, Downloaded from https://agupubs.onlinelibrary.wiley.com/doi/10.1029/2022WR031938 by Office Of Scientific And Technical Information, Wiley Online Library on [29/08/2023]. See the Terms and Conditions (https://onlinelibrary.wiley.com/terms-and-conditions) on Wiley Online Library for rules of use; OA articles are governed by the applicable Creative Commons License

19447973, 2022, 9, Downloaded from https://agupubs.onlinelibrary.wiley.com/doi/10.1029/2022WR031938 by Office Of Scientific And Technical Information, Wiley Online Library on [29/08/2023]. See the Terms and Conditions (https://onlinelibrary.wiley.com/terms-and-conditions) on Wiley Online Library for rules of use; OA articles are governed by the applicable Creative Commons License

The repeatability of main characteristics of the process for 3 grain glass cylinders at lower separations (such as those listed above), namely: the upper contact tilt onset time, meniscus acceleration onset time, and the length of the jump is within about 13% on average (see also Guével et al., 2020, for a wider perspective on capillary bridge rupture of spherical and cylindrical, both glass and Teflon grains).

5. Conclusions

Morphing of capillary water between three glass cylinders during its evaporation and the involved kinematics are quite complicated as they depend on a series of multi-physical, mutually coupled processes. Drying of a granular medium consists of a slow phase controlled by the evaporation rate, intercalated by unstable jumps lasting tens of seconds or less, but leading to a complete reconfiguration of the water mass and ending with another slow phase. While these occurrences have been known for a long time at a mesoscale, here we bring new observations at the sub-grain scale.

What are the conditions for the transition between the slow and fast phase, is the first question to be answered. The presented analysis focuses on the geometry of the water body and its kinematics. Using cylinders in the experiments allows one to observe the meniscus evolution in an almost two-dimensional form, with a one-dimensional curvature. The latter allows one to assess the changes in capillary pressure during evaporation. The instabilities, recognizable as related to Haines jumps, or reons, constitute, what is known as air entry in unsaturated soil mechanics at a continuum scale, and a precursor to macroscopic drying-cracking.

The initial phase of meniscus propagation is at the rate commensurate with that of the evaporation rate. The first instability starts shortly before the tip of the RHS meniscus approaches the location of throat, which is at the shortest distance between the surfaces of the neighboring solid grains. The meniscus starts as a segment of a near-circle, becoming sharper and sharper as its tip approaches the throat. It originally is about 80 μm in depth, but increases to 147 μm, when the instability starts. The jump is of the order 600 μm. The second singularity occurs when the RHS meniscus approaches the LHS bottom grain surface and consists of a split of the RHS meniscus into two, the first one, between the two LHS grains, and the second one, between the two bottom grains. This results in a switch of the bottom contact from the RHS to the LHS cylinder. It is preceded by a practically ceasing advancement of the lower contact point of the RHS meniscus.

It is noted that the radius of curvature is rarely uniform across the meniscus in contradiction of the Laplace-Young hypothesis in the case of the 2D capillary bridge. The interplay of different areas of the meniscus, that is, the contact area and the central tip area, results into an initial sharpening and then flattening of the meniscus at the midsection when crossing the area of throat and subsequently evolving into the jump instability. The evolution of the capillary water body and menisci is likely linked to the configuration of the solid grain boundaries. Finally, the resulting gradients of curvature are expected to lead to micro-flows of liquid within the bridge, as has been assessed for pendular bridges by Yang et al. (2018). Such micro-flows are yet to be quantified.

One of the implications of the sub-grain scale findings regarding meniscus kinematics and morphology concerns upscaling the meniscus to the level of a drying front. One possible way to upscale is via averaging (e.g., Armstrong et al., 2015; Bear, 1972; Berg et al., 2013; Georgiadis et al., 2011), other ways include using experiments and simulations on synthetic structured materials with percolation approach or dissipation extremization (de Gennes, 1976; Leseur et al., 2021; Veveakis & Regenauer-Lieb, 2015). It is expected that the front propagation rate at a larger scale depends on the proportions between evaporation and instability driven segments of the displacement of menisci, both in terms of space and time. Other forms of front propagation have been observed experimentally at a macroscale, such as cooperative pore filling (Berg et al., 2013) and/or transformation of air entry into a drying crack (e.g., Holtzman & Juanes, 2010; Hueckel et al., 2014). Phase field technique appears to be an attractive tool for moving phase-transition interfaces (see Guével et al., 2020).

Viewing the meniscus evolution at a mesoscale, as in Hueckel et al., 2020 and Mielniczuk et al., 2021, one concludes from the presented observations that the progress of the drying front occurs in its two-third, roughly, via micropulses of the Haines jumps. As for the events of meniscus split, the top contact does not really participate in a jump. For the bottom contact, two-third of its progress is through the jump, and one-third via the steady evaporation, as far as distances are concerned. Thus, less than half of the progress of the drying front at this scale occurs as a result, and with the rate of evaporation, while more than half of the progress consists of instability

jumps, with the rate orders of magnitude higher. Consequently, understanding the frequency of the jumps at a sub-grain scale is crucial for the kinematics of the drying front and its modeling at a macroscale.

From an engineering point of view, it is of interest to identify any precursors of the instability. As the first precursor, one may identify the tilting of the top liquid/solid contact toward one side (RHS), when the contact velocity starts visibly increasing above the value controlled by evaporation alone. The second precursor is cessation on that (RHS) side (and only that side) of the stick and slip (rocking) pattern of the contact motion.

Clearly, one of the questions arising at this point is about the cause of the instability of the meniscus. It has been repeatedly and likely correctly argued before, that the first instability arises at the throat, where the meniscus needs first to squeeze through, but then spread out rapidly. From the presented data of the geometric/kinematic measurements, it appears that the instability starts before the meniscus contact points approach the throat. We observe that the meniscus accelerates when its tip relaxes after having passed the throat, while the lagging contact points are still to be further squeezed closer. A continuity of such an evolution would constitute a departure from the equilibrium condition as defined by Laplace law, specifically the postulated equality of the curvature radius along the entire meniscus. The dynamic aspects of those circumstances, and specifically, the force conditions for the jump, are likely linked to the lack of equilibrium configurations, while the evaporation-driven meniscus advances. These aspects are presented in Hueckel et al. (2022).

Appendix A

Three main steps are necessary in further processing of the data: adjustment and preprocessing of recorded images (with use of ImageJ), image processing (Matlab) and correlation of reconstructed variables with measured capillary force (Matlab).

First, images are adjusted, cropped, and rotated (if needed). Then, functions “Threshold” and “Find Edges” are used to transform source images into 2-color images, with white edges (color 1) on black background (color 0). So, prepared images are saved as GIF files and are subsequently digitalized in a Matlab code. An example of an image preparation and of reconstructed images for front and side views are presented in Figure A1.

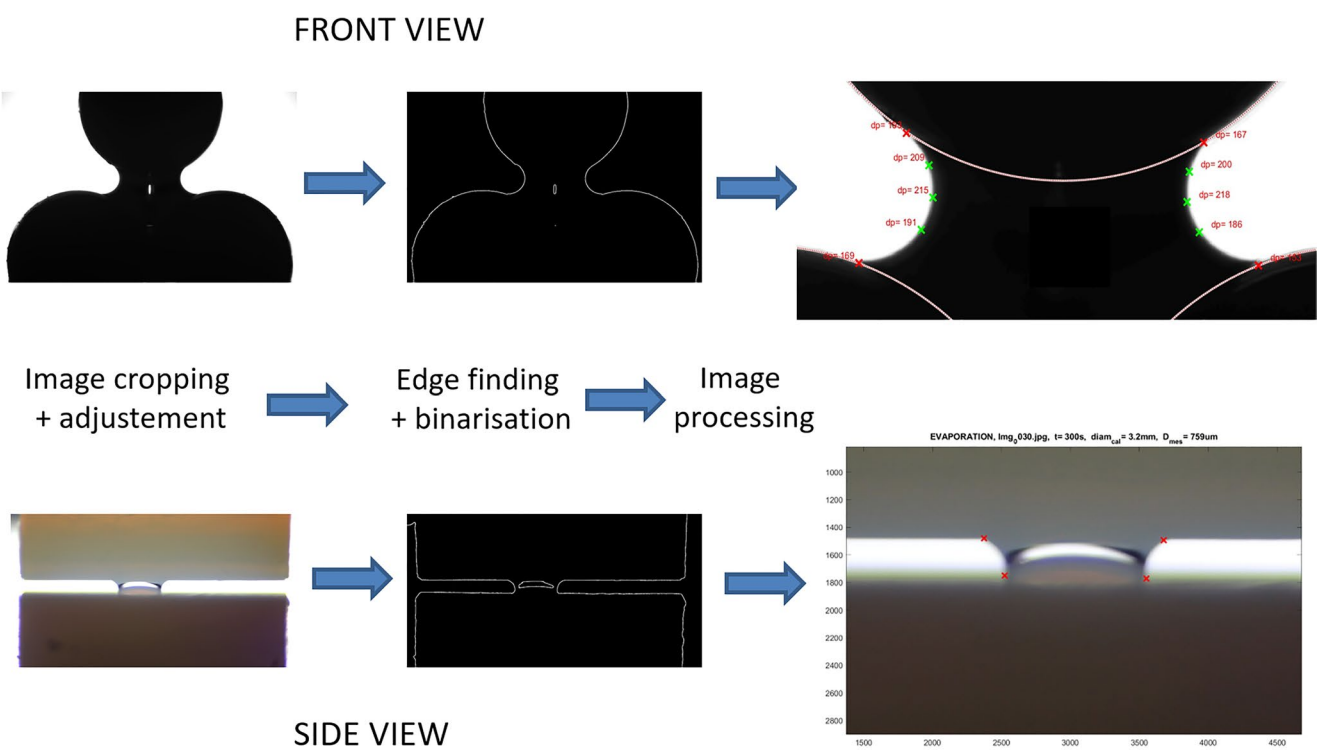

Figure A1. Image preparation and processing sequence.

19447973, 2022, 9, Downloaded from https://agupubs.onlinelibrary.wiley.com/doi/10.1029/2022WR031938 by Office Of Scientific And Technical Information, Wiley Online Library on [29/08/2023]. See the Terms and Conditions (https://onlinelibrary.wiley.com/terms-and-conditions) on Wiley Online Library for rules of use; OA articles are governed by the applicable Creative Commons License

To process images using the prepared code, some initial parameters are needed. These are:

- The upper cylinder diameter and length, measured with the use of calipers, which are necessary to calibrate the length units (from pixels to meters) and to adapt the side view images.
- The identification of region of interest (ROI) for both views—rectangular regions containing the grain edges and capillary profiles (see Figure A2a).
- The identification of auxiliary parameters, which are used to increase the precision of the reconstruction.

For each time step, both images (front and side view) are processed. At first, all (x and y) coordinates of points on upper and lower grains edges are determined in defined ROI and circles are fitted using these coordinates, yielding the values for the centers and radii of the upper and lower grains $Par_{1\text{-}3}$ (x,y,r). Subsequently, the coordinates of points on the bridge profile are identified inside the ROI window, by scanning line-by-line (Y-coordinates) the ROI, determining the left (minimum X value for the given line) and the right (maximum X value for the given line) bridge profile, yielding a set of (x and y) coordinates of all points on the left and right profiles. Only the points which are outside the reconstructed grains are kept as the bridge profile. In the nearest vicinity of the reconstructed grains, the bridge profiles (ends) are approximated by a linear fit.

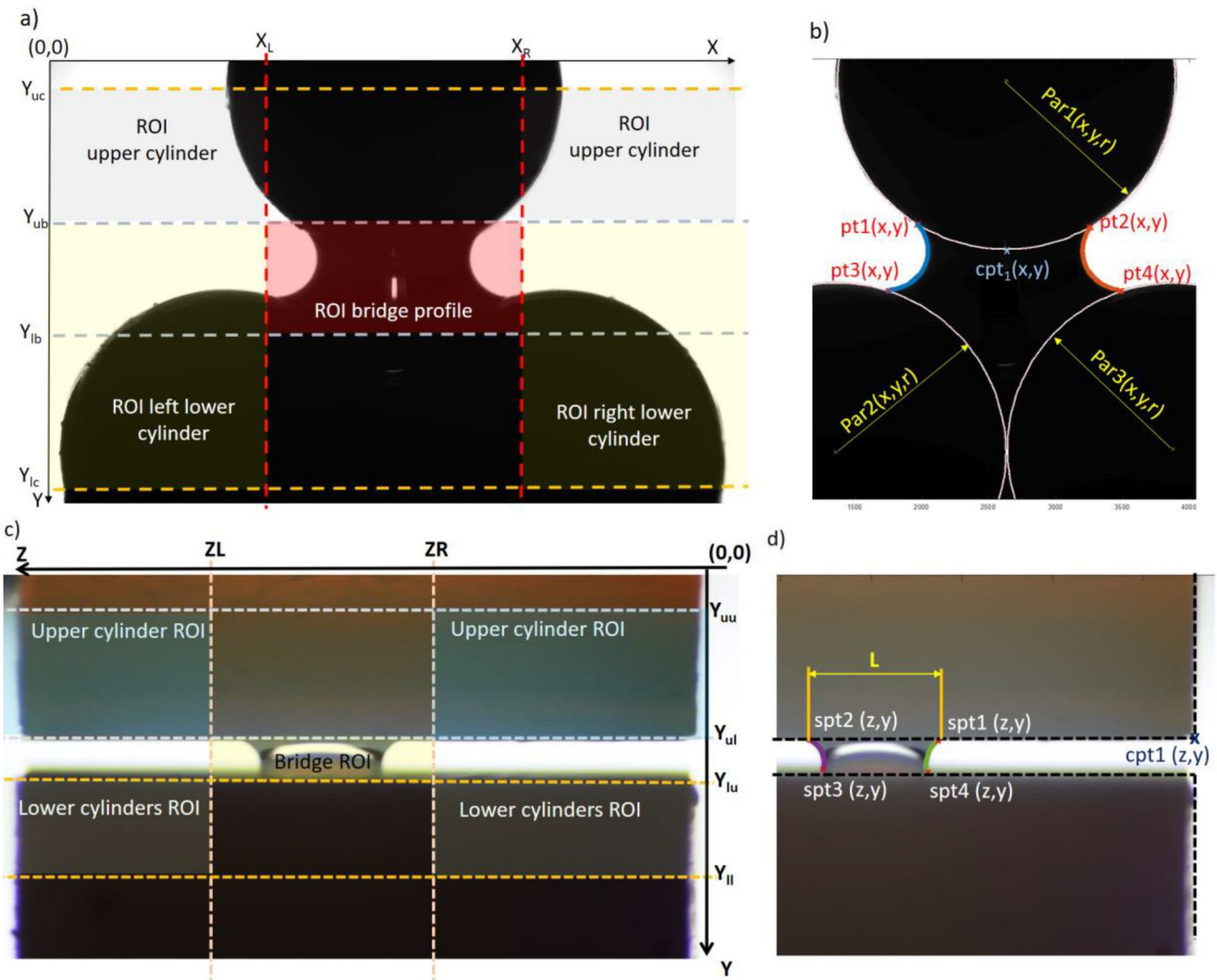

Figure A2. Definition of regions of interest for the front view (a) and the side view (c), reconstructed main variables for the front view (b) and the side view (d).

19447973, 2022, 9, Downloaded from https://agupubs.onlinelibrary.wiley.com/doi/10.1029/2022WR031938 by Office Of Scientific And Technical Information, Wiley Online Library on [29/08/2023]. See the Terms and Conditions (https://onlinelibrary.wiley.com/terms-and-conditions) on Wiley Online Library for rules of use; OA articles are governed by the applicable Creative Commons License

19447973, 2022, 9, Downloaded from https://agupubs.onlinelibrary.wiley.com/doi/10.1029/2022WR031938 by Office Of Scientific And Technical Information, Wiley Online Library on [29/08/2023]. See the Terms and Conditions (https://onlinelibrary.wiley.com/terms-and-conditions) on Wiley Online Library for rules of use; OA articles are governed by the applicable Creative Commons License

Having the coordinates of the points on both profiles, the coordinates of contact points pt1 (x,y)-pt4 (x,y) are determined, as the first and the last points on the reconstructed bridge profiles. The lowest point of the upper cylinder is needed to correlate the front and side views, as it is the only point visible on both views.

The main variables obtained during the processing of the front view photos are identified in Figure A2b.

Similar techniques are used for the reconstruction of grains and bridge profiles in the side view. At first, the coordinates of the points on the edges of the upper grain, lower grain, and bridge profiles are determined inside the identified ROIs. The length of the upper cylinder is measured from the image, and then used with the length measured with the caliper, to calibrate the length units (pixels per meter). The lowest point of the upper cylinder, cpt1, is a common point between side and front view. Based on this point, the side image is transformed and resized to keep the same coordinates and units as in the front view, to have the same units for x, y, and z coordinates. For the samples with a higher separation of grains, it is possible to determine four contact points: spt1, spt2, spt3, spt4, and upper and lower bridge length. For the lower separations, the liquid bridge is not perfectly visible on the side view and only its overall length may be estimated.

Data Availability Statement

The raw experimental data and the processing software are available at a public repository at https://osf.io/e465m/.

Acknowledgments
The authors acknowledge funding from the US DOE NEUP grant DE-NE0008746.

References

AECL. (1997). The buffer/container experiment: Results, synthesis, issues, AECL-11746, COG-97–46-I.

Armstrong, R. T., Evseev, N., Koroteev, D., & Berg, S. (2015). Modeling the velocity field during Haines jumps in porous media. *Advances in Water Resources*, *77*, 57–68. https://doi.org/10.1016/j.advwatres.2015.01.008

Armstrong, S., McHale, G., Ledesma-Aguilar, R., & Wells, G. G. (2019). Pinning-free evaporation of sessile droplets of water from solid surfaces. *Langmuir*, *35*(8), 2989–2996. https://doi.org/10.1021/acs.langmuir.8b03849

Bear, J. (1972). *Dynamics of fluids in porous media*. Elsevier.

Benvegnú, F., Brondi, A., & Polizzano, C. (1988). Natural analogues and evidence of long-term isolation capacity of clays occurring in Italy. CEC Report EUR 11896.

Berg, S., Ott, H., Klapp, S. A., Schwing, A., Neiteler, R., Brussee, N., et al. (2013). Real-time 3D imaging of Haines jumps in porous media flow. *Proceedings of the National Academy of Sciences of the United States of America*, *110*(10), 3755–3759. https://doi.org/10.1073/pnas.1221373110

Bormashenko, E., Musin, A., & Zinigrad, M. (2011). Evaporation of droplets on strongly and weakly pinning surfaces and dynamics of the triple line. *Colloids and Surfaces A Physicochemical and Engineering Aspects*, *385*(1), 235–240. https://doi.org/10.1016/j.colsurfa.2011.06.016

de Gennes, P. G. (1976). La percolation: Un concept unificateur. *La recherche*, *7*(72), 919–27.

Fisher, R. A. (1926). On the capillarity forces in an ideal soil; correction of formulae given by W. B. Haines. *Journal of Agricultural Science*, *16*(3), 492–505. https://doi.org/10.1017/s0021859600007838

Gagneux, G., Millet, O., Mielniczuk, B., & El Youssoufi, M. S. (2017). Theoretical and experimental study of pendular regime in unsaturated granular media. *European Journal of Environmental and Civil Engineering*, *21*(7–8), 840–853. https://doi.org/10.1080/19648189.2016.1167782

Georgiadis, A., Berg, S., Maitland, G., & Ott, H. (2011). *Pore-scale micro-CT imaging: Non-wetting phase cluster size distribution during drainage and imbibition* (pp. 18–21). InternationalSymposium of the Society of Core Analysts (SCA).

Gera, F., Hueckel, T., & Peano, A. (1996). Critical issues in modelling the long-term hydro-thermo- mechanical performance of natural clay barriers. *Engineering Geology*, *41*(1–4), 17–33. https://doi.org/10.1016/0013-7952(95)00047-x

Guével, A., Rattez, H., & Veveakis, E. (2020). Viscous phase-field modeling for chemo-mechanical microstructural evolution: Application to geomaterials and pressure solution. *International Journal of Solids and Structures*, *207*, 230–249. https://doi.org/10.1016/j.ijsolstr.2020.09.026

Haines, W. B. (1928). Capillary properties of moist granular media. *Nature*, *122*(3077), 607–608. https://doi.org/10.1038/122607a0

Hedan, S., Cosenza, P., Valle, V., Dudoignon, P., Fauchille, A.-L., & Cabrera, J. (2012). Investigation of the damage induced by desiccation and heating of Tournemire argillite using digital image correlation. *International Journal of Rock Mechanics and Mining Sciences*, *51*, 64–75. https://doi.org/10.1016/j.ijrmms.2012.01.001

Holtzman, R., & Juanes, R. (2010). Crossover from fingering to fracturing in deformable disordered media. *Physical Review E—Statistical Physics, Plasmas, Fluids, and Related Interdisciplinary Topics*, *82*(4), 046305. https://doi.org/10.1103/physreve.82.046305

Hu, H., & Larson, R. G. (2005). Analysis of the microfluid flow in an evaporating sessile droplet. *Langmuir*, *21*(9), 39623–3971. https://doi.org/10.1021/la047528s

Hueckel, T., Kaczmarek, M., & Caramuscio, P. (1997). Theoretical assessment of fabric and permeability changes in clays affected by organic contaminants. *Canadian Geotechnical Journal*, *34*(4), 588–603. https://doi.org/10.1139/t97-013

Hueckel, T., Mielniczuk, B., & El Youssoufi, M. S. (2020). Adhesion-force micro-scale study of desiccating granular material. *Géotechnique*, *70*(12), 1133–1144. https://doi.org/10.1680/jgeot.18.P.298

Hueckel, T., Mielniczuk, B., El Youssoufi, M. S., Hu, L. B., & Laloui, L. (2014). A three-scale cracking criterion for drying soils. *Acta Geophysica*, *62*(5), 1049–1059. https://doi.org/10.2478/s11600-014-0214-9

Hueckel, T., Mielniczuk, B., Guével, A., & Veveakis, M. (2022). Capillary water in 2-D drying—Cracking soil sub-grain models: Dynamics and Instabilities of evaporation and Haines jumps, *a companion paper (WRR)*. https://doi.org/10.1029/2022WR031938

Hueckel, T., & Pellegrini, R. (2002). Reactive plasticity for clays: Application to a natural analog of long-term geomechanical effects of nuclear waste disposal. *Engineering Geology*, *64*(2–3), 195–215. https://doi.org/10.1016/s0013-7952(01)00114-4

Joanny, J.-F., & De Gennes, P.-G. (1984). A model for contact angle hysteresis. *The Journal of Chemical Physics*, *81*(1), 552–562. https://doi.org/10.1063/1.447337

Laplace, P. S. (1805). Traité de mécanique céleste. *Supplément au dixième livre du Traité de Mécanique Céleste*, *4*, 1–79.

Le Sueur, M., Poulet, T., & Veveakis, M. (2021). Predicting the yield strength of a 3D printed porous material from its internal geometry. *Additive Manufacturing*, *44*, 102061. https://doi.org/10.1016/j.addma.2021.102061

Ma, C. M., & Hueckel, T. (1992). Stress and pore pressure in saturated clay subjected to heat from radioactive-waste—A numerical-simulation. *International Journal of Engineering Science*, *30*(11), 1567–1582. https://doi.org/10.1016/0020-7225(92)90126-2

Mayor, J.-C., Velasco, M., & Garcia-Sineriz, J.-L. (2007). Ventilation experiment in the Mont Terri underground laboratory. *Physics and Chemistry of the Earth*, *32*(8–14), 616–628. https://doi.org/10.1016/j.pce.2006.04.030

Melnikov, K., Mani, R., Wittel, F. K., Thielmann, M., & Herrmann, H. J. (2015). Grain-scale modeling of arbitrary fluid saturation in random packings. *Physical Review E*, *92*(2), 022206. https://doi.org/10.1103/physreve.92.022206

Melrose, J. C. (1970). Interfacial phenomena as related to oil recovery mechanisms. *Canadian Journal of Chemical Engineering*, *48*, 638–644.

Mielniczuk, B., El-Youssoufi, M. S., & Hueckel, T. (2021). The mechanics of air entry of drying-cracking soils: Physical models. *Computers and Geotechnics*, *136*, 104177. https://doi.org/10.1016/j.compgeo.2021.104177

Mielniczuk, B., El Youssoufi, M. S., Sabatier, L., & Hueckel, T. (2014b). Rupture of an evaporating liquid bridge between two grains. *Acta Geophysica*, *62*(5), 1087–1108. https://doi.org/10.2478/s11600-014-0225-6

Mielniczuk, B., Hueckel, T., & El Youssoufi, M. S. (2015). Laplace pressure evolution and four instabilities in evaporating two-grain liquid bridges. *Powder Technology*, *283*, 137–151. https://doi.org/10.1016/j.powtec.2015.05.024

Mielniczuk, B., Hueckel, T., & El Youssoufi, M. S (2014). Evaporation-induced evolution of the capillary force between two grains. *Granular Matter*, *16*(5), 815–828. https://doi.org/10.1007/s10035-014-0512-6

Moebius, F., & Or, D. (2012). Interfacial jumps and pressure bursts during fluid displacement in interacting irregular capillaries. *Journal of Colloid and Interface Science*, *377*, 406–415. https://doi.org/10.1016/j.jcis.2012.03.070

Morrow, N. R. (1970). Irreducible wetting-phase saturations in porous media. *Chemical Engineering Science*, *25*(11), 1799–I815. https://doi.org/10.1016/0009-2509(70)80070-7

Peron, H., Laloui, L., Hu, L. B., & Hueckel, T. (2013). formation of drying crack patterns in soils: A deterministic approach. *Acta Geotechnica*, *8*(2), 215–22. https://doi.org/10.1007/s11440-012-0184-5

Peron, H., Laloui, L., Hueckel, T., & Hu, L. B. (2009). Desiccation cracking of soils. *European Journal of Environmental and Civil Engineering*, *13*(7–8), 869–888. https://doi.org/10.3166/ejece.13.869-888

Richefeu, V., El Youssoufi, M. S., Azema, E., & Radjai, F. (2009). Force transmission in dry and wet granular media. *Force transmission in dry and wet granular media*, *190*(1–2), 258–263. https://doi.org/10.1016/j.powtec.2008.04.069

Scardovelli, R., & Zaleski, S. (1999). Direct numerical simulation of free-surface and interfacial flow. *Annual Review of Fluid Mechanics*, *31*(1), 567–603. https://doi.org/10.1146/annurev.fluid.31.1.567

Scherer, G. W. (1992). Crack-tip stress in gels. *Journal of Non-Crystalline Solids*, *144*, 210–216. https://doi.org/10.1016/S0022-3093(05)80402-8

Semprebon, C., Scheel, M., Herminghaus, S., Seemann, R., & Brinkmann, M. (2016). Liquid morphologies and capillary forces between three spherical beads. *Physical Review E*, *94*(1), 012907. https://doi.org/10.1103/physreve.94.012907

van der Heijden, T. W. G., Darhuber, A. A., & van der Schoot, P. (2018). Macroscopic model for sessile droplet evaporation on a flat surface. *Langmuir*, *34*(41), 12471–12481. https://doi.org/10.1021/acs.langmuir.8b02374

Veveakis, E., & Regenauer-Lieb, K. (2015). Review of extremum postulates. *Current Opinion in Chemical Engineering*, *7*, 40–6. https://doi.org/10.1016/j.coche.2014.10.006

Wang, J.-P., Gallo, E., François, B., Gabrieli, F., & Lambert, P. (2017). Capillary force and rupture of funicular liquid bridges between three spherical bodies. *Powder Technology*, *305*, 89–98. https://doi.org/10.1016/j.powtec.2016.09.060

Yang, S., Mielniczuk, B., El Youssoufi, M. S., & Hueckel, T. (2018). A note on evolution of pressure and flow within evaporating capillary bridge. *European Physical Journal E: Soft Matter*, *41*(12), 140. https://doi.org/10.1140/epje/i2018-11748-x

Young, T. (1805). An essay on the cohesion of fluids. *Philosophical Transactions of the Royal Society of London*, *95*, 65–87. https://doi.org/10.1098/rstl.1805.0005

Zhao, B., MacMinn, C. W., Primkulov, B. K., Chen, Y., Valocchi, A. t. J., Zhao, J., et al. (2019). Comprehensive comparison of pore-scale models for multiphase flow in porous media. *Proceedings of the National Academy of Sciences of the United States of America*, *116*(28), 13799–13806. https://doi.org/10.1073/pnas.1901619116

Zhao, C.-F., Kruyt, N. P., & Millet, O. (2020). Capillary bridges between spherical particles under suction control: Rupture distances and capillary forces. *Powder Technology*, *360*, 622–634. https://doi.org/10.1016/j.powtec.2019.09.093

19447973, 2022, 9, Downloaded from https://agupubs.onlinelibrary.wiley.com/doi/10.1029/2022WR031938 by Office Of Scientific And Technical Information, Wiley Online Library on [29/08/2023]. See the Terms and Conditions (https://onlinelibrary.wiley.com/terms-and-conditions) on Wiley Online Library for rules of use; OA articles are governed by the applicable Creative Commons License